



# Overall subshear but locally supershear rupture of the 2021 $M_w$ 7.4 Maduo earthquake from high-rate GNSS waveforms and three-dimensional InSAR deformation

Mingzhe Lyu, Kejie Chen\*, Changhu Xue, Nan Zang, Wei Zhang, Guoguang Wei

*Department of Earth and Space Sciences, Southern University of Science and Technology, Shenzhen 518055, China*

## ARTICLE INFO

### Keywords:

2021  $M_w$  7.4 Maduo earthquake  
High-rate GNSS waveforms  
3D deformation  
Locally supershear

## ABSTRACT

An  $M_w$  7.4 left-lateral earthquake hit Maduo County in Qinghai province, China, on 21 May 2021. In this paper, we combined the 1-Hz global navigation satellite system (GNSS) displacement waveforms, GNSS static offsets and the three-dimensional (3D) co-seismic deformation field from the interferometric synthetic radar (InSAR) measurements to estimate the source kinematics of this event. Our results reveal that there was about 160 km of surface ruptures with varying strike angles, and the earthquake propagated bilaterally, with the bulk of the slip formed to the southeast of the epicenter. Substantial slip occurred to a depth of ~6 km, and the estimated maximum slip was ~5 m. The source time function presents a ~35-s total duration with two peaks, and the total geodetic seismic moment is  $1.61 \times 10^{20}$  Nm (equivalent to  $M_w$  7.4). The near-field high-rate GNSS waveforms inversion results indicate that this earthquake is an overall subshear but locally supershear rupture event. The preferred average rupture velocity is 2.8 km/s while the velocities to the southeast and northwest of epicenter are 3.8 and 2.2 km/s, respectively. Supershear enhanced ground motion and simulation using the 3D curvilinear grid finite-difference method shows the acceleration caused by the earthquake exceeded the building code limits for bridges that collapsed due to strong ground shaking. Furthermore, this earthquake increased the stress level of the Maqin–Maqu segment of the East Kunlun Fault, and was also responsible for an off-fault aftershock sequence at the northwest end of the earthquake rupture.

## 1. Introduction

As one of the most active tectonic blocks in the Tibetan Plateau, the Bayan Har block has hosted more than 20 earthquakes of  $\geq M_w$  7 (Fig. 1) over the last 100 years. Nearly all the damaging events have been concentrated along the boundaries of the block, e.g., the 2001  $M_w$  7.8 East Kunlun earthquake along the East Kunlun Fault to the north and the 2008  $M_w$  7.9 Wenchuan earthquake along the Longmen Shan Fault to the east. The spatial clustering of these earthquakes seems to support the view of a rigid block motion model (e.g., Avouac and Tappomier, 1993), which would thus shape the seismic potential assessment and seismic hazard preparation in the area (Wang et al., 2021b). However, large earthquakes have also been found to occur inside the Bayan Har block, with one documented case being the  $M_w$  7.7 Dari earthquake in 1947, which ruptured the Dari Fault with ~150 km of surface deformation (from the geomorphological investigation by Dai, 1983). However, detailed information about the source of the  $M_w$  7.7 Dari earthquake

remains unknown, due to the very limited near-field records at that time.

On May 21, 2021, another large earthquake of  $M_w$  7.4 struck the interior of the Bayan Har block. The epicenter was located in Maduo County, Qinghai province (<http://www.ceic.ac.cn/history>), ~180 km to the northwest of the 1947  $M_w$  7.7 Dari earthquake. The focal mechanism solution provided by the Global Centroid-Moment-Tensor (GCMT) project (Ekström et al., 2012) indicated that it was a sub-vertical left-lateral strike-slip event with a relatively shallow centroid depth (12 km). In addition, the field survey by Gai et al. (2021) found ~151 km of tortuous surface rupture, distributed mainly along the Kunlun–shankou–Jiangcuo Fault, which is a southern branch of the East Kunlun Fault zone. No casualties were reported, but this earthquake did cause significant damage to nearby bridges (Guan et al., 2021). Since there was no strong motion station deployed in the epicentral area, it is difficult to characterize the ground shaking in the near-source region for bridge damage analysis. Alternatively, the ground motion can be estimated using a kinematic rupture model constrained by co-seismic

\* Corresponding author.

E-mail address: [chenkj@sustech.edu.cn](mailto:chenkj@sustech.edu.cn) (K. Chen).

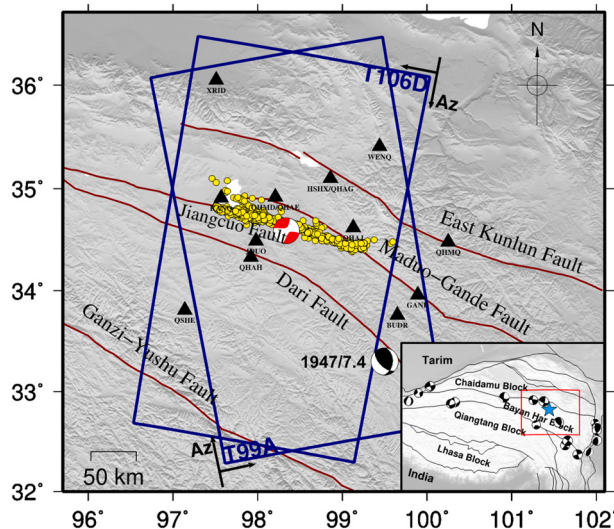


**Fig. 1.** Tectonic setting map for the 2021  $M_w$  7.4 Maduo earthquake. The red focal mechanism shows the Global Centroid-Moment-Tensor solution for this seismic event, the black beach ball is the 1947  $M_w$  7.7 Dari earthquake, and the black triangles indicate the GNSS stations used in the slip inversion. The yellow dots indicate the distribution of the aftershock sequences. The blue rectangle outlines the coverage of the ascending and descending InSAR images used in this study. The insert map indicates that the study area is located within the Bayan Har block in the northeastern part of the Qinghai-Tibet Plateau. The red rectangle marks the study area. The blue star denotes the epicenter, and the black focal mechanism shows the 20 earthquakes of  $\geq M_w$  7 that have occurred on the Bayan Har block over the last 100 years. (For interpretation of the references to colour in this figure legend, the reader is referred to the web version of this article.)

observations.

The source kinematics of the  $M_w$  7.4 Maduo earthquake have been explored independently by the use of static global navigation satellite system (GNSS) offsets (e.g., Li et al., 2021; Wang et al., 2021a, 2021b) and interferometric synthetic aperture radar (InSAR) line-of-sight (LOS) measurements (e.g., Jin and Fialko, 2021; Zhao et al., 2021), and also by the use of joint datasets (e.g., Chen et al., 2022; Zhang et al., 2022a). The slip distributions obtained from inversions of the GNSS co-seismic displacements are quite similar in both Li et al. (2021) and Wang et al. (2021a, 2021b), with both studies reporting two asperities: a larger one to the northwestern end of the rupture fault and a smaller one to the southeastern end. There were very marginal slips between the two asperities, and the peak slips ruptured all the way from 10-km depth to the surface. In contrast, thanks to the dense spatial coverage, the InSAR data revealed at least five asperities, but the maximum slip did not approach the surface, implying shallow slip deficit (SSD), as demonstrated in many previous studies (e.g., Fialko et al., 2005; Xu et al., 2016; Jin and Fialko, 2021).

The 2021  $M_w$  7.4 Maduo earthquake caused up to 2.8 m of surface rupture (Gai et al., 2021), which inevitably led to coherence loss for the radar interferograms in the near-fault area. As demonstrated by Xu et al. (2016), the incomplete data coverage close to the fault zone tends to result in overestimation of the SSD, which in turn causes underestimation of the ground shaking. The pixel offset tracking (POT), including the range and azimuth offsets, can provide the near-field co-seismic displacements. Furthermore, many strike-slip events tend to rupture at very fast velocities (Wang et al., 2016), while Zhang et al. (2022a) demonstrated a supershear signal from back-projection, such a feature was missing in Chen et al. (2022) using high-rate GNSS waveforms.

In this study, we first used the ascending and descending Sentinel-1 synthetic aperture radar (SAR) images spanning the pre- and post-seismic period, and applied differential interferometric SAR (DInSAR) and pixel offset tracking (POT) methods to obtain the co-seismic

deformation. Based on the 1-Hz GNSS displacement waveforms, GNSS static offsets and the three-dimensional (3D) displacements from SAR observations, we obtained the detailed rupture history for the 2021  $M_w$  7.4 Maduo earthquake. We further discussed the source model difference between our preferred model and published studies. Specially, we highlighted the rupture characteristics of overall subshear but locally supershear from near field GNSS waveforms. Finally, we modeled the strong ground motion using a grid-based finite-difference method and calculated the static Coulomb failure stress (CFS) changes of the surrounding faults, to assess the risk of future earthquake disasters in this area.

## 2. Three-dimensional co-seismic deformation from Sentinel-1 observations

### 2.1. InSAR data processing

We utilized a pair of Sentinel-1 A/B radar images on descending track 106 and a pair of Sentinel-1 A/B images on ascending track 99 to obtain the co-seismic deformation, which were both used in Terrain Observation with Progressive Scans (TOPS) mode. The detailed InSAR data information is summarized in Table 1.

GMTSAR software (Sandwell et al., 2011) was employed to process the SAR images. We utilized the precise orbit information downloaded from ESA's Sentinel-1 quality control website (<https://s1qc.asf.alaska.edu/>) to achieve the co-registration of the master and slave SAR images. The 30-m resolution Shuttle Radar Topography Mission (SRTM) digital elevation map (DEM) (Farr et al., 2007) was used to remove the topographic signal. We then filtered the interferograms using a Gaussian filter with a wavelength of 200 m and specified the number of multi-looks in the range and azimuth directions as 8:2, following Vaka et al. (2020), which can suppress the phase noise and improve the signal-to-noise ratio (SNR). Decorrelated areas were masked using the nearest-neighbor interpolation algorithm (Agram and Zebker, 2009), based on stacked coherence, and then the statistical-cost, network-flow algorithm for phase unwrapping software (Chen and Zebker, 2000) was used to unwrap the interferograms to the LOS displacement field. Finally, we geocoded all the interferograms to the geographic coordinates. However, the Sentinel-1 interferometric phase can be decorrelated around the rupture trace (Xu et al., 2016), so we employed the POT method in the open-source Jet Propulsion Laboratory InSAR Scientific Computing Environment (ISCE) software (Rosen et al., 2012) to obtain the range and azimuth offsets.

Fig. 2 shows the six obtained co-seismic SAR deformation fields. In order to meet the geometric requirements of 3D displacement estimation, the azimuth offsets (Fig. 2c, f) with low SNR cannot be excluded, as they help constrain the N-S component of the displacement field (Fialko et al., 2001). However, we do need to eliminate the large outliers in the azimuth offsets to avoid distortion of the final 3D deformation field. According to the LOS differential measurements (Fig. 2a, d), the absolute value of the maximum surface deformation caused by the earthquake was no more than 2 m, so we first eliminated the azimuth offset data points where the absolute value was greater than 2 m. After the above processing, there were still singular points and we then performed median filtering processing on the azimuth offsets.

**Table 1**  
InSAR data information.

Track	Master date	Slave date	Perp (m)	Incident angle (°)	Azimuth angle (°)	Standard deviation (cm)
T99A	2021/05/20	2021/05/26	56.92	39.5	-10.1	0.56
T106D	2021/05/20	2021/05/26	118.29	39.5	190.1	0.60

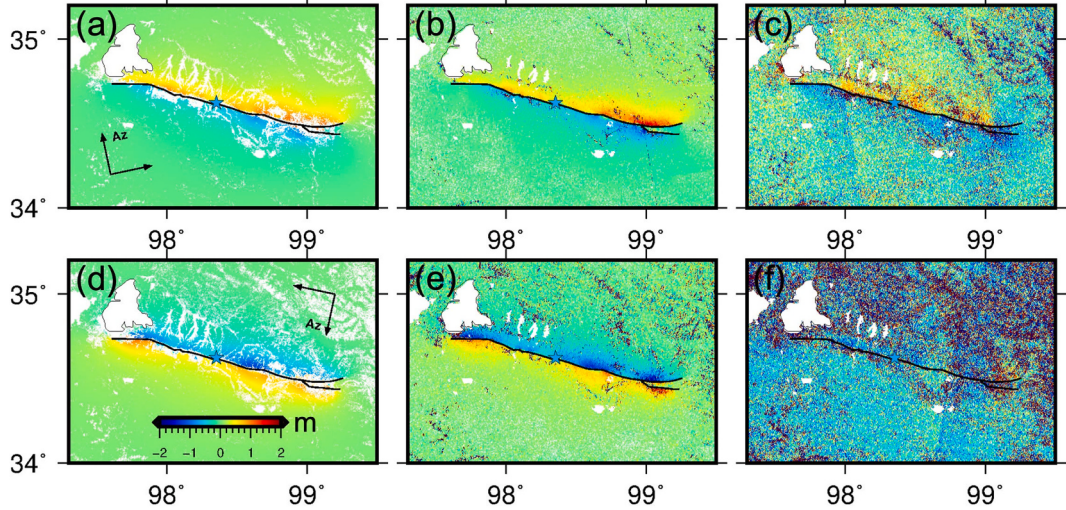


**Fig. 2.** Co-seismic displacement fields. (a), (b), and (c) represent Sentinel-1 ascending track T99A. (d), (e), and (f) represent descending track T106D. (a) and (d) are the LOS deformation based on the DInSAR method, (b) and (e) are the range offsets, and (c) and (f) are the azimuth offsets. Black arrows denote the radar azimuth and range directions, and the black lines are the rupture fault traces. The blue star denotes the epicenter. (For interpretation of the references to colour in this figure legend, the reader is referred to the web version of this article.)

## 2.2. Three-dimensional displacement field estimation using the TR-ESISTEM approach

Guglielmino et al. (2011) proposed the simultaneous and integrated strain tensor estimation from geodetic and satellite deformation measurements (SISTEM) method, based on elasticity theory, which estimates the 3D deformation by integrating GNSS and InSAR data. Its solution also provides a strain tensor and rigid body rotation tensor solution. Luo and Chen (2016) proposed an extended SISTEM method (ESISTEM), which enables the surrounding InSAR measurement to be used to constrain the derived deformation, based on the theory of surface elasticity. Mehrabi et al. (2019) reported that the application of Tikhonov regularization in the process of solving 3D displacements can obtain a stable solution. We then further applied Tikhonov regularization (Tikhonov et al., 2013) to the ESISTEM method, and propose the Tikhonov-regularized ESISTEM (TR-ESISTEM) method to reduce the distortion of the points to be sought caused by the dramatic changes in the surrounding deformation points, to obtain a stable solution.

According to continuum mechanics, we can calculate the deformation at the point of interest based on the deformation around it, under the hypothesis of infinitesimal and homogeneous elastic strain field (Pietrantonio and Riguzzi, 2004; Borre, 2007; Guglielmino et al., 2011). We assume that a point of interest is P, and its coordinates and displacements are  $x^P = (x_e^P, x_n^P, x_v^P)$  and  $u^P = (u_e^P, u_n^P, u_v^P)$ . There are then N experimental points around point P, and the coordinates and displacements of the i-th point are expressed as  $x^i = (x_e^i, x_n^i, x_v^i)$  and  $u^i = (u_e^i, u_n^i, u_v^i)$ . The first-order Taylor series expansion of  $u^i$  can then be built as:

$$u^i = H_{ij} \Delta x^j + u^P, i = 1, 2, \dots, N \quad (1)$$

where  $\Delta x^j = x^j - x^P$ , denoting the vector distance component from the i-th experimental point to point P.  $H_{ij}$  is the displacement gradient tensor, which can be expressed as the sum of the symmetric strain tensor  $\varepsilon_{ij}$  and antisymmetric rigid body rotation tensor  $\omega_{ij}$ :

$$H_{ij} = \varepsilon_{ij} + \omega_{ij} = \begin{bmatrix} \varepsilon_{11} & \varepsilon_{12} & \varepsilon_{13} \\ \varepsilon_{12} & \varepsilon_{22} & \varepsilon_{23} \\ \varepsilon_{13} & \varepsilon_{23} & \varepsilon_{33} \end{bmatrix} + \begin{bmatrix} 0 & -\omega_3 & \omega_2 \\ \omega_3 & 0 & -\omega_1 \\ -\omega_2 & \omega_1 & 0 \end{bmatrix} \quad (2)$$

In a simplified form, Eq. (1) can be expressed by the following linear relationship:

$$u = A \cdot l \quad (3)$$

where  $l = [u_e^P \ u_n^P \ u_v^P \ \varepsilon_{11} \ \varepsilon_{12} \ \varepsilon_{13} \ \varepsilon_{22} \ \varepsilon_{23} \ \varepsilon_{33} \ \omega_1 \ \omega_2 \ \omega_3]^T$  denotes the unknown parameter vector at point P, and  $u = [u_e^1 \ u_n^1 \ u_v^1 \dots u_e^N \ u_n^N \ u_v^N]$  represents the displacement vector observed at the N surrounding experimental points. A is a  $3N \times 12$  coefficient matrix, which can be expressed as:

$$A = \begin{bmatrix} 1 & 0 & 0 & \Delta x_e^1 & \Delta x_n^1 & \Delta x_v^1 & 0 & 0 & 0 & 0 & 0 & \Delta x_v^1 & -\Delta x_n^1 \\ 0 & 1 & 0 & 0 & \Delta x_e^1 & 0 & \Delta x_n^1 & \Delta x_v^1 & 0 & 0 & -\Delta x_v^1 & 0 & \Delta x_e^1 \\ 0 & 0 & 1 & 0 & 0 & \Delta x_e^1 & 0 & \Delta x_n^1 & \Delta x_v^1 & \Delta x_n^1 & -\Delta x_e^1 & 0 & 0 \\ \dots & \dots \\ \dots & \dots \\ 1 & 0 & 0 & \Delta x_e^N & \Delta x_n^N & \Delta x_v^N & 0 & 0 & 0 & 0 & 0 & \Delta x_v^N & -\Delta x_n^N \\ 0 & 1 & 0 & 0 & \Delta x_e^N & 0 & \Delta x_n^N & \Delta x_v^N & 0 & 0 & -\Delta x_v^N & 0 & \Delta x_e^N \\ 0 & 0 & 1 & 0 & 0 & \Delta x_e^N & 0 & \Delta x_n^N & \Delta x_v^N & \Delta x_n^N & -\Delta x_e^N & 0 & 0 \end{bmatrix} \quad (4)$$

where  $\Delta x_j^i = x_j^i - x_j^P$  ( $j = e, n, v; i = 1, 2, \dots, N$ ) is the distance between the i-th experimental point and point P in direction j. In addition, there are also geodetic observations at point P, for which the unit vectors are considered to be  $(S_e^P, S_n^P, S_v^P)$ , so the corresponding coefficient matrix is  $A^P = [S_e^P \ S_n^P \ S_v^P \ 0 \ 0 \ 0 \ 0 \ 0 \ 0 \ 0 \ 0 \ 0 \ 0]$ . If we suppose that the observed displacement at point P is  $u^P$ , then the relationship between the unknown parameter vector at point P and the observations at point P can be similarly expressed as:

$$u^P = A^P \cdot l \quad (5)$$

Eqs. (3) and (5) can then be combined as:

$$\begin{pmatrix} u \\ u^P \end{pmatrix} = \begin{pmatrix} A \\ A^P \end{pmatrix} l \quad (6)$$

Eq. (6) is the function model for calculating the 3D deformation based on the ESISTEM method. Following Hu et al. (2014), the 3D displacement maps can be reconstructed by combining the LOS (equal to the range) and the azimuth measurements from at least two different tracks. In this study, the surrounding observations  $u$  include the LOS and the azimuth displacements of the ascending and descending from DInSAR and POT, and the observations  $u^P$  at point P include all observations mentioned above. Eq. (6) can be briefly expressed by Eq. (3), the least-squares solution of which can be expressed as:

$$l = (A^T W A)^{-1} A^T W u \quad (7)$$

where  $W$  is the observation weight matrix. Here, we introduce Tikhonov regularization (Tihonov, 1963) to stabilize the inversion. If we suppose that  $\|\cdot\|_{L_2}$  is the Euclidean L2 norm and  $\alpha$  is the regularization factor determined through the L-curve criterion (Hansen, 1992), then the objective function (Hansen, 1990) becomes:

$$\min(\|Al - u\|_{L_2}^2 + \alpha\|l\|_{L_2}^2) \quad (8)$$

The Tikhonov-regularized solution to Eq. (3) is solved as:

$$l_{reg} = (A^T W A + \alpha I)^{-1} A^T W u \quad (9)$$

where  $I$  is the identity matrix, for which the variance-covariance matrix can be expressed as:

$$C_{l_{reg}} = (A^T W A + \alpha I)^{-1} \quad (10)$$

### 2.3. Results

Using the TR-ESISTEM algorithm, we obtained the 3D deformation field (see Fig. 3) for the Maduo earthquake from the six InSAR images, for which the accuracy was further evaluated by the co-seismic offsets at 21 GNSS stations. The root-mean-square errors (RMSEs) in the E-W, N-S, and vertical components are 2.49 cm, 13.09 cm, and 4.22 cm, respectively. The relatively poor precision of the N-S component can be expected as it results from the low-quality azimuth observations obtained through POT technology. In the E-W displacement map, a symmetrical southeast–northwest strike plane is formed between the coseismic offsets, while the characteristic of symmetrical offsets on both sides of the fault disappears in the N-S displacement map, and there is an obvious southern offset to the southeastern end of the fault. The surface rupture traces drawn from the 3D displacements is close to the field survey (Fig. 3a) from Ren et al. (2022). According to the rupture traces, we can see that the strike of the fault changes a lot at both ends, and it is not a straight line in the middle part of the fault, which indicates complicated ruptures caused by the 2021  $M_w$  7.4 Maduo earthquake.

The 3D displacement fields (Fig. 3) show that there are quite a few noise points in the far field, while the deformation is relatively smooth in the east–west and vertical directions of the near field. Due to the relationship between the offsets’ range and azimuth resolution and the seismic deformation (Jin and Fialko, 2021), the SNR in the near field is high, while the SNR in the far field is low. Therefore, it was necessary to remove the far-field displacements of the 3D deformation before it could be used for inversion. We used the quadtree method (Jónsson et al.,

2002) to downsample the 3D displacements in the designated area of the near field (Fig. 4), which can not only reduce the amount of InSAR data points in the slip inversion process, but can also retain more deformation points in the high gradient deformation areas. Please note this approach is sensitive to high-frequency noise and tends to yield more points in far-field noisy areas, which could affect the inversion results. Therefore, we only reserved the deformation points near the fault and increased the gradient threshold for window partition to reduce the influence of this sampling method on the inversion result.

## 3. Finite fault slip inversion

### 3.1. Modeling method

We jointly used the static offsets (including the InSAR-derived near-fault 3D deformation and GNSS static displacements) and 1-Hz GNSS displacement waveforms provided by Chen et al. (2022) to perform the inversion for the slip distribution. The fault orientation was set following the surface trace imaged from InSAR, and the best-fitting dip angle 80° was determined through grid search, i.e., we varied the GCMT dip angle (87°) between 77° and 90° with a step of 1°. We eventually constructed a fault model composed of 837 sub-patches, each with a dimension of 2 km × 2 km. The hypocenter (98.3541° E, 34.6242° N, 8.0 km) was manually adjusted based on the solution from the China Earthquake Networks Center, to ensure that the high-rate GNSS waveforms fitted well.

Based on the Crust1.0 crustal velocity model (Laske et al., 2013, see Table S1), we synthesized the elastostatic and elastodynamic Green’s function using the frequency-wavenumber integration method developed by Zhu and Rivera (2002). Each subfault was parametrized with six 50% overlapping windows, and the time window was depicted by a 3-s duration triangle-shaped slip rate function. To account for rake-varying ruptures, we considered a 50° window around the −9° rake of GCMT solution and adopted two slip vectors with rake angles of −34° and 16° at each patch. In addition, we applied a non-negative least-squares method (Lawson and Hanson, 1995) to ensure that the direction of the inverted slip vector was positive. Slip inversion is an ill-posed problem, and we employed the spatial Laplacian regularization (Hartzell and Heaton, 1983) and the temporal first derivative regularization to constrain the inversion (Melgar Moctezuma, 2014), with the optimal smoothing parameters selected according to Akaike’s Bayesian information criterion (ABIC) (Akaike, 1980) (see Fig. S4). The determination of optimal rupture velocities is clarified in Section 4.2.

Relative weighting assignment is quite tricky in joint inversion and is a still going research topic. To the best of our knowledge, there is no rule

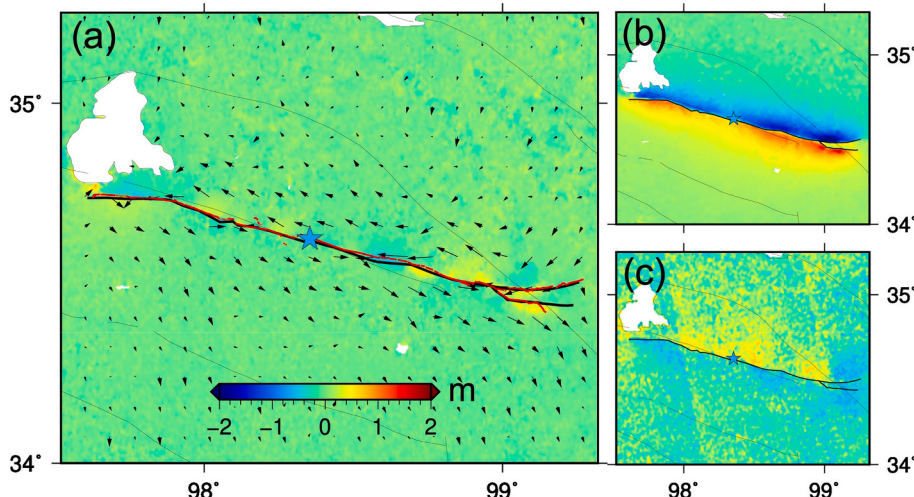


**Fig. 3.** 3D co-seismic deformation map for the 2021 Maduo earthquake. (a), (b), and (c) represent the vertical, E-W, and N-S displacements, respectively. The blue star denotes the epicenter, and the vector arrows in (a) represent the direction of the horizontal deformation. The black curved lines are the fault traces, and the red lines in (a) are the field survey rupture traces from Ren et al. (2022). (For interpretation of the references to colour in this figure legend, the reader is referred to the web version of this article.)

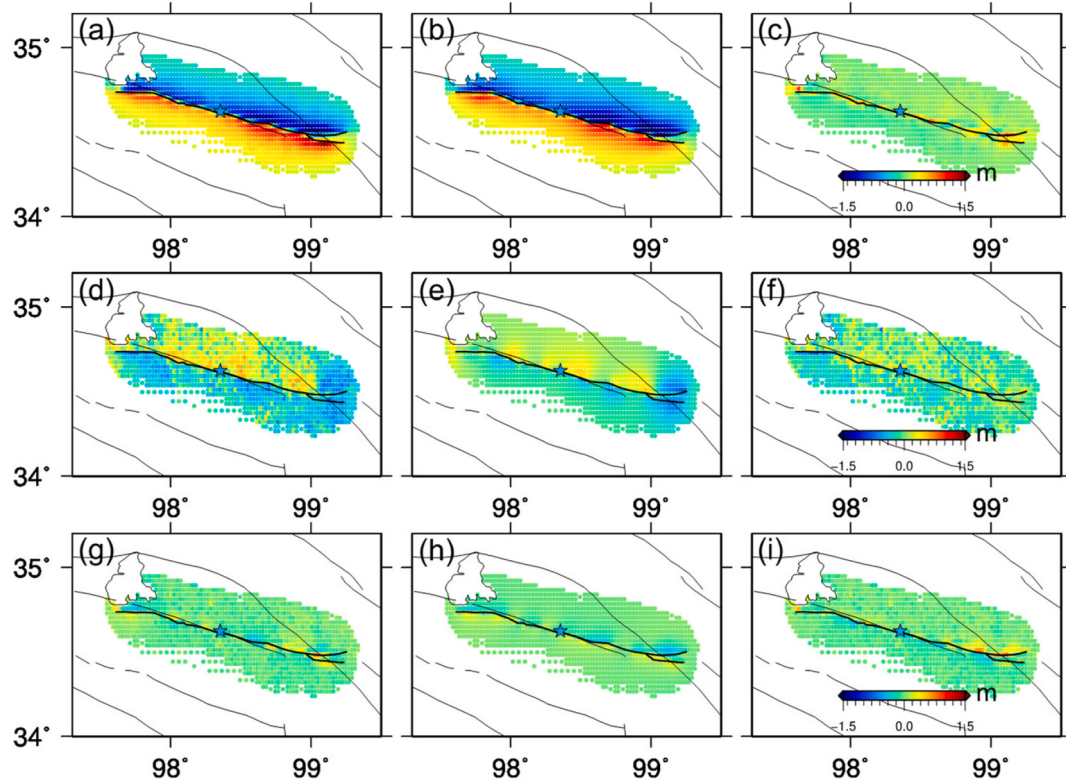


**Fig. 4.** Observations (left panel), fits (middle panel), and residuals (left panel) of the 3D displacements. From top to bottom are the north-south, east-west, and up-down components, respectively. The blue star denotes the epicenter, and the black lines are the fault surface traces. (For interpretation of the references to colour in this figure legend, the reader is referred to the web version of this article.)

of thumb to follow currently. For example, while Wang and Fialko (2014) proposed an objective method to determine weights among ALOS and Envisat observations, other researchers (e.g., Melgar et al., 2020; Yue et al., 2020) prefer trial and error. In this study, we initially determined the relative weight ratio among these observations based on the RMSEs of the 3D displacements, the errors of the GNSS static offsets, and the standard deviation of each high-rate GNSS recording. We then obtained the optimal weight ratio (Table S2) among the GNSS static offsets, high-rate GNSS, east-west, north-south and vertical InSAR 3D components by trial and error, to ensure that each dataset was fitted well.

### 3.2. Slip model

The preferred model (Fig. 5b) shows that the maximum slip amplitudes are inferred in the depth interval of 4–6 km, above the hypocenter depth (8 km), with less than 4-m slip between the 2-km depth and the surface. The earthquake propagated bilaterally yet ruptured asymmetrically, and the major asperities, together with the estimated ~5 m peak slip, were formed to the southeast of the epicenter. Furthermore, the inverted rake angles show predominantly strike-slip motion with marginal normal components, consistent with the GCMT focal mechanism. From 16 s to 20 s, there was a clear decrease in the slip rate due to the change of the strike direction, which would hinder the rupture propagation, and was responsible for the two-peaked source time function. In total,  $1.61 \times 10^{20}$  Nm seismic moment (equivalent to  $M_w$  7.4) was released within 35 s.

The optimal slip model fits the GNSS static offsets and displacement waveforms generally well (Fig. 6), with variance reductions (VRs) of 93.6% and 79.7%. As for the 3D measurements (Fig. 4), the VR of the E-W, N-S, and vertical components is 97.6%, 76.9%, and 40.5%, respectively. The lower VR of the vertical component appears to be a result of the relatively low weight ratio in the slip inversion and the

smaller value compared with the horizontal displacements, since this event was a dominant left-lateral strike-slip event.

A jackknife test (Kim and Dreger, 2008) was carried out for each patch, to estimate the slip uncertainty. We repeated the inversion about 100 times after randomly removing 20% of the dataset. The coefficient of variation (CV) of the slip is the ratio between the standard deviation (Std.) of the slip and the mean slip. The result (Fig. 7) shows that the CV in the main slip area is less than 0.2, which suggests that the slip in this area is stable and the inversion result is reliable. The larger standard deviation of the westernmost segment may be related to the spatial distribution of the observation. The InSAR data were missing on the northern side of the westernmost segment because there is a lake in the area where InSAR could not be imaged. Besides, higher values of CV are mainly concentrated in the depth, indicating both poor resolution from the surface measurements and little slip there (Melgar et al., 2015).

In order to investigate the resolution of the joint inversion, we also conducted a checkerboard test, through building a synthetic checkerboard slip distribution and simulating all the data used in this inversion. The results (Fig. S1) show that the shallow slip (0–10 km) can be reliably recovered, while the deep slip (10–20 km) can be partially recovered.

## 4. Discussion

### 4.1. Comparisons with published slip models

A few slip models have been published for the 2022 M7.4 Maduo earthquake. To fit the InSAR measurements, L. He et al. (2021) used 6 faults with varying dip angles, and their maximum slip was ~5 m, consistent with our result, yet the slip distribution is relatively concentrated and there was no significant void between the main asperities, but slip gaps between the four main asperities can be clearly identified in our results. Besides, the asperity to the northwest in their model is much deeper than ours. The maximum slip inverted by Guo et al. (2021) is

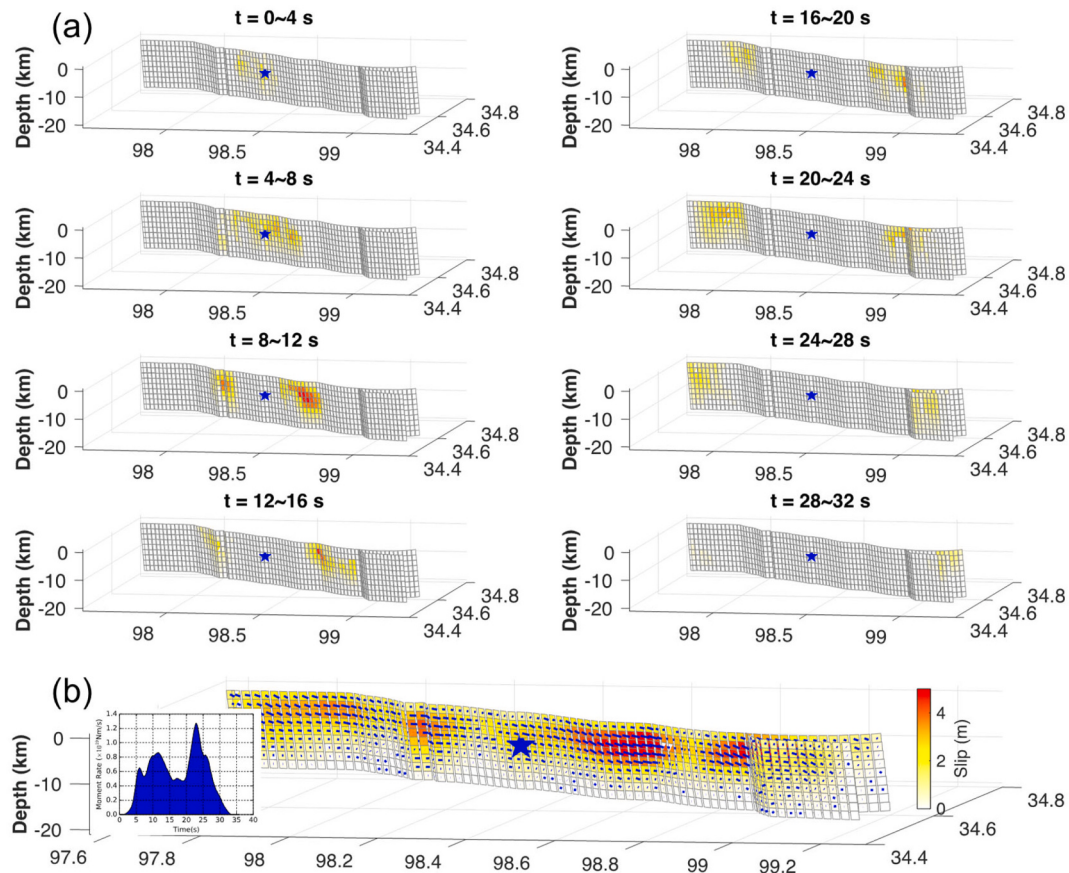


**Fig. 5.** (a) The rupture evolution for the preferred slip model at 4-s intervals, where the blue star indicates the epicenter. (b) The preferred slip model inverted from the 3D displacements and 1-Hz GNSS waveforms. The blue lines on the fault patches indicate the slip directions, and the blue star denotes the epicenter. The insert map is the source time function. (For interpretation of the references to colour in this figure legend, the reader is referred to the web version of this article.)

surprisingly as large as 9.3 m, and the slip distribution on the branch faults to the southeast is deeper than our results. These differences in slip amplitude and depth are probably attributed to the choice of smoothing factors and poor resolution of InSAR data at depth.

Zhang et al. (2022a) performed a joint inversion by InSAR, teleseismic and strong motion observations using only three rectangular faults, and their results reveal that the slip depth is almost the same for the southeast and northwest segments, which is also the case of Chen et al. (2022) from InSAR and high-rate GNSS waveforms. In our optimal rupture model, slip concentration to the southeast reaches 10 km while to the northwest it is less than 6 km, similar to Yue et al. (2022). Discrepancy in slip amplitude and depth may correspond to different prestress levels that accounts for different rupture velocities (Brumhat et al., 2016) as discussed in Section 4.2.

#### 4.2. Overall subshear but locally supershear rupture

Chen et al. (2022) determined a rupture velocity of 2.6–2.8 km/s by fitting high-rate waveforms at 14 local GNSS stations, and they suspected there was no supershear component through analyzing the fault normal and parallel displacement waveforms. However, back-projection results (e.g., Li et al., 2022; Zhang et al., 2022a) indicate that the 2022  $M_w$  7.4 Maduo earthquake indeed involved supershear rupture. In this study, through assuming a constant rupture velocity, we also get the best data match at 2.8 km/s or about 0.8 times of shear wave velocity (see the corresponding waveform fits in Fig. S2) and hence this earthquake should be categorized as an overall subshear event from this perspective. We then test different rupture velocities ranging from 1.6 to 4.8 km/s with a step of 0.2 km/s on each side of the epicenter, and grid search

results of GNSS displacement waveform fits against rupture velocities are shown in Fig. 8a.

Our optimal model from iterations shows distinctly different rupture velocities to the southeast (3.8 km/s) and northwest (2.2 km/s) of epicenter, which is similar to the back-projection results (Li et al., 2022; Zhang et al., 2022a). Compared with the constant rupture velocity model, VR was improved to 4.52%. To highlight the mismatch of near-field GNSS waveforms under different rupture velocities, we present waveform fitting (see Fig. 8b and c) at two GNSS stations QHAJ and KANQ which are closest to the fault. As clearly demonstrated, synthetic waveforms at the two stations are mainly sensitive to rupture velocity on its own side, thus making it difficult to separate subshear and supershear signatures when a constant rupture velocity is assumed.

#### 4.3. Strong ground motion modeling

Ground motion modeling plays a significant role in earthquake engineering and rapid damage estimation, based on the preferred slip model, we simulated strong ground motion in the presence of an irregular free surface using the 3D version of the curvilinear grid finite-difference method developed by Zhang and Chen (2006). The model was made up of the surface topography from the GTOPO30 DEM (<https://www.usgs.gov/centers/eros/science/usgs-eros-archive-digital-elevation-global-30-arc-second-elevation-gtopo30>) and the 3D structure from the Crust1.0 crustal model (Laske et al., 2013). The velocity model was discretized with  $800 \times 567 \times 700$  grid cells in the fault-parallel, fault-normal, and vertical directions, respectively. The horizontal grid spacing was 300 m and the vertical grid spacing was 100 m. These modeling parameters provide reliable synthetic waveforms up to  $\sim 0.3$

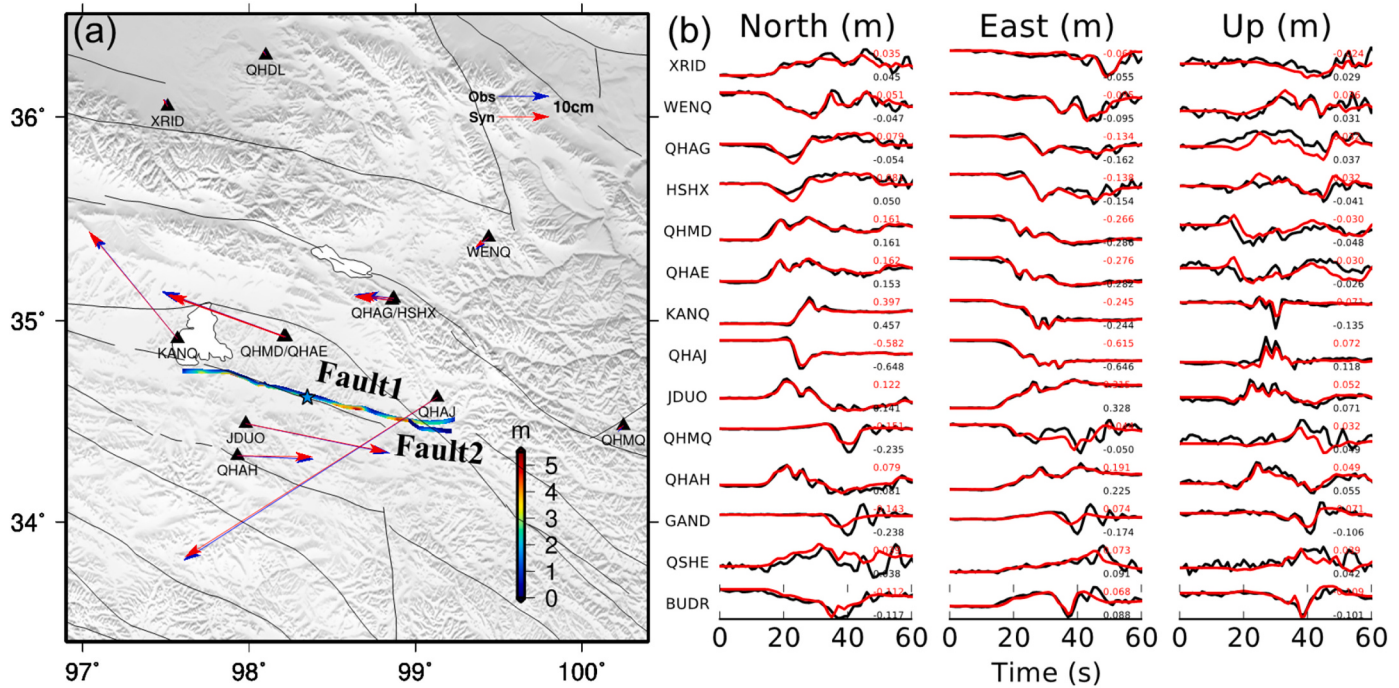


**Fig. 6.** (a) The slip distribution projected onto the surface. The blue star denotes the location of the epicenter. The black and red arrows indicate the static GNSS observations and simulations from the preferred slip model in the horizontal direction. (b) The synthetic waveforms of the preferred slip model fitted to the high-rate GNSS waveforms. The synthetic and observed waveforms are shown as red and black lines, and the number of each waveform is the peak amplitude. (For interpretation of the references to colour in this figure legend, the reader is referred to the web version of this article.)

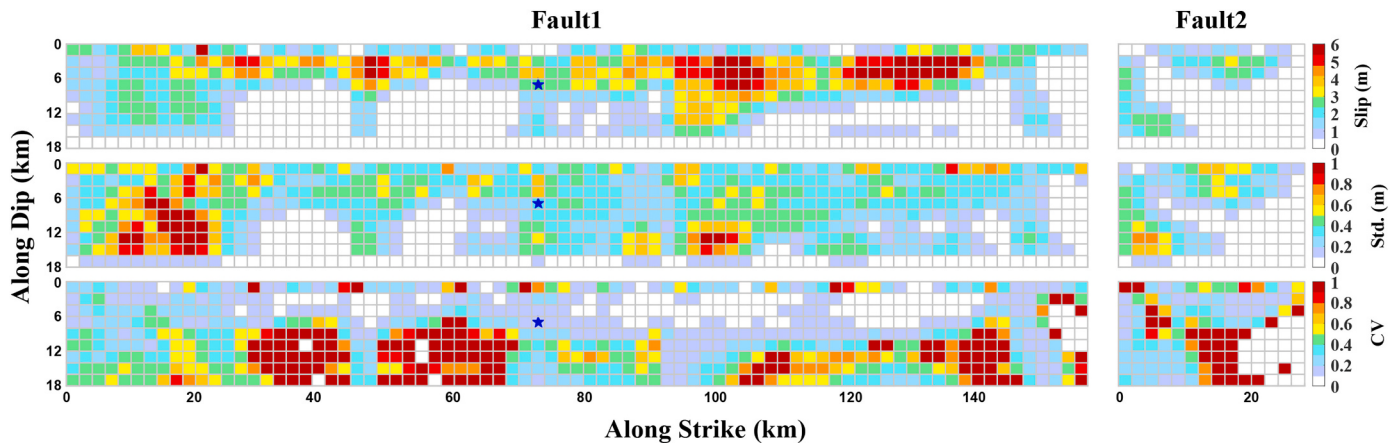


**Fig. 7.** Jackknife test of randomly removing 20% of the dataset 100 times, with the mean slip model (top), the standard deviation (middle), and the coefficient of variation (bottom). Fault 1 is the main curve fault, and Fault 2 is a secondary curve fault to the southeast of the epicenter. Both are denoted in Fig. 6a. The blue star presents the epicenter. (For interpretation of the references to colour in this figure legend, the reader is referred to the web version of this article.)

Hz. The time increment in the calculation was 0.01 s, and the total number of time increments was 10,000, which corresponds to a 100-s wave propagation.

Fig. 9 shows the peak ground acceleration (PGA) and seismic intensity distributions. These snapshots characterize the strong ground shaking of the Maduo earthquake, and are generally consistent with the preliminary results of the field survey (Gai et al., 2021; Guan et al., 2021). As indicated by the snapshot of the peak ground motion, the strongest shaking occurred above the hanging wall of the fault. The PGA for the Changma River Bridge, Yamatan Bridge, and No. 2 Yamantan Bridge was 2.756 m/s<sup>2</sup>, 2.3348 m/s<sup>2</sup>, and 1.8620 m/s<sup>2</sup>, respectively, which exceeds the specifications for the seismic design of highway bridges in 2020 (Ministry of Transportation of China, 2020).

#### 4.4. Variations of the Coulomb stress in neighboring faults

The Coulomb stress changes can be resolved on to receiver faults with specified rake direction and geometry (Lin and Stein, 2004). To investigate the stress variations in the neighboring strike-slip faults caused by this earthquake, we further calculated the Coulomb stress failure  $\Delta CFS$  changes with a 3D elastic dislocation model (Feng et al., 2017; Okada, 1992) following:

$$\Delta CFS = \Delta\tau + \mu' \Delta\sigma_n \quad (11)$$

where  $\Delta\tau$  and  $\Delta\sigma_n$  are the changes in shear force and normal stress on the fault plane induced by the earthquake.  $\mu'$  is the effective friction coefficient. Here, we set  $\mu'$  to 0.4, according to the research of King et al.

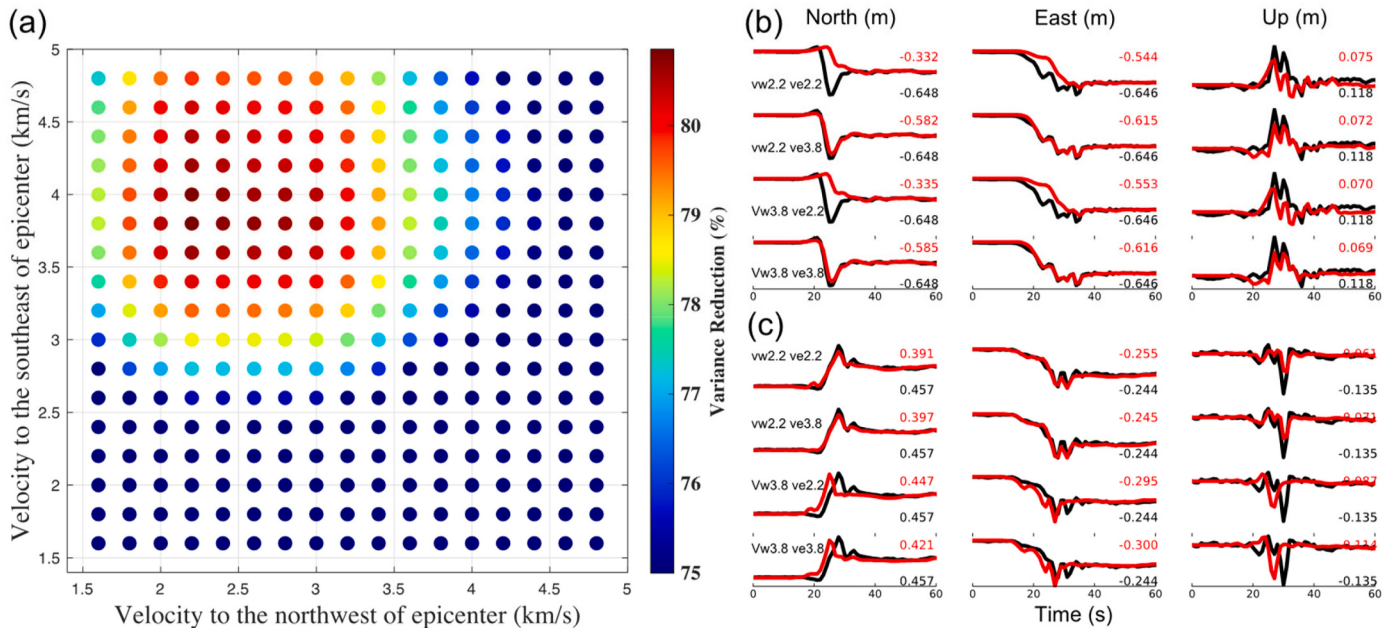


**Fig. 8.** (a) Variance reductions of GNSS displacement waveform against rupture velocities on both sides of the epicenter. (b) and (c) are the waveform fitting of QHAJ and KANQ stations, respectively. The synthetic and observed waveforms are shown as red and black lines, and the number on the right side of each waveform is the peak amplitude. (For interpretation of the references to colour in this figure legend, the reader is referred to the web version of this article.)

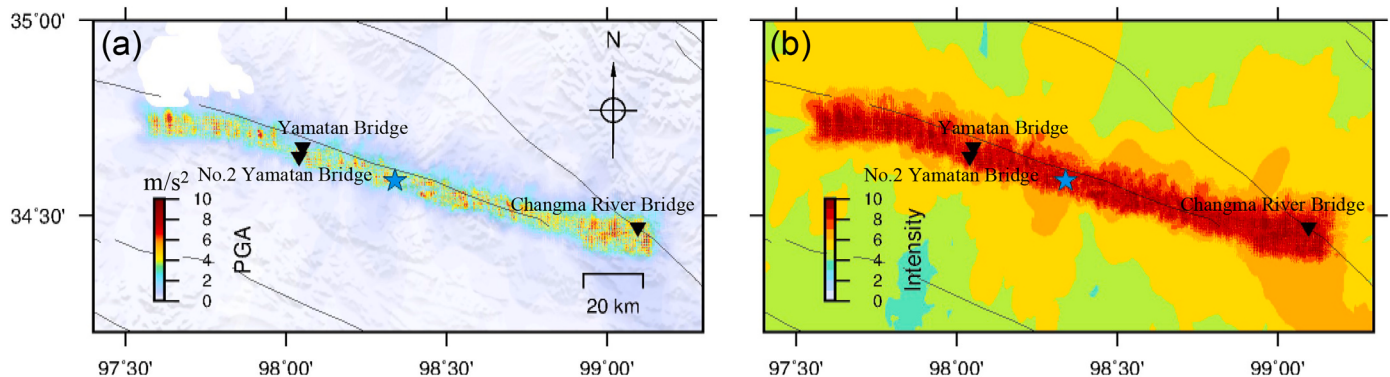


**Fig. 9.** (a) Distribution of the peak ground acceleration (PGA, m/s<sup>2</sup>). (b) Seismic intensity map for the  $M_w$  7.4 earthquake. The inverted triangles indicate the locations of the three damaged bridges, and the blue star represents the epicenter. (For interpretation of the references to colour in this figure legend, the reader is referred to the web version of this article.)

(1994). Based on the average orientation of seismogenic fault, we set strike, dip and rake of receiver faults as  $292^\circ$ ,  $80^\circ$  and  $0^\circ$  to calculate the Coulomb stresses at a depth of 10 km. We then applied variable strike angles of the receiver faults to calculate the Coulomb stresses on the four adjacent faults.

On the one hand, the  $M_w$  7.4 Maduo earthquake caused a Coulomb stress increase of  $\geq 0.1$  bars in the Maqin–Maqu and the eastern Tuosuo Lake segments of the East Kunlun Fault zone (Fig. 10a). The Maqin–Maqu segment is considered to be a seismic gap on the East Kunlun Fault (Wen et al., 2007), and the stress loading on this segment was increased by several historical earthquakes and the post-seismic viscoelastic relaxation process (Shan et al., 2015). Our results show that the 2021 Maduo earthquake also had an effect on the stress accumulation in the Maqin–Maqu segment, so that the future large earthquake potential in the Maqin–Maqu seismic gap is considerable. On the other hand, there was a significant Coulomb stress decrease in the central-southern segment of the Dari Fault and Maduo–Gande Fault, and part of the East Kunlun Fault, thereby delaying the occurrence of future earthquakes. Overall, the  $M_w$  7.4 Maduo earthquake released the stress

accumulation in the northeastern part of the Bayan Har block, to some extent, and increased the stress loading on part of the East Kunlun Fault, especially the Maqin–Maqu segment.

Furthermore, the aftershock relocation results (Wang et al., 2021b; Zhang et al., 2022b) indicate a possible fault branch to the northwest of the main fault, but no evident surface deformation was detected by the InSAR interferograms, and it remains unclear whether a co-seismic rupture exists at depth or the aftershocks were driven by the Coulomb stress increase. Based on the 3D displacements, GNSS static offsets and high-rate GNSS waveforms, we used the fault model with and without this extra fault to perform sensitivity tests, respectively. The results show that the fitting of the three data sets does not change significantly, and there was no slip distribution found during the co-seismic whether the fault was retained (see Fig. S3). Furthermore, despite releasing the Coulomb stress on the fault plane at 0–10 km, the  $M_w$  7.4 mainshock increased the Coulomb stress at 10–25 km (Fig. 10b), which is consistent with the aftershock depth.

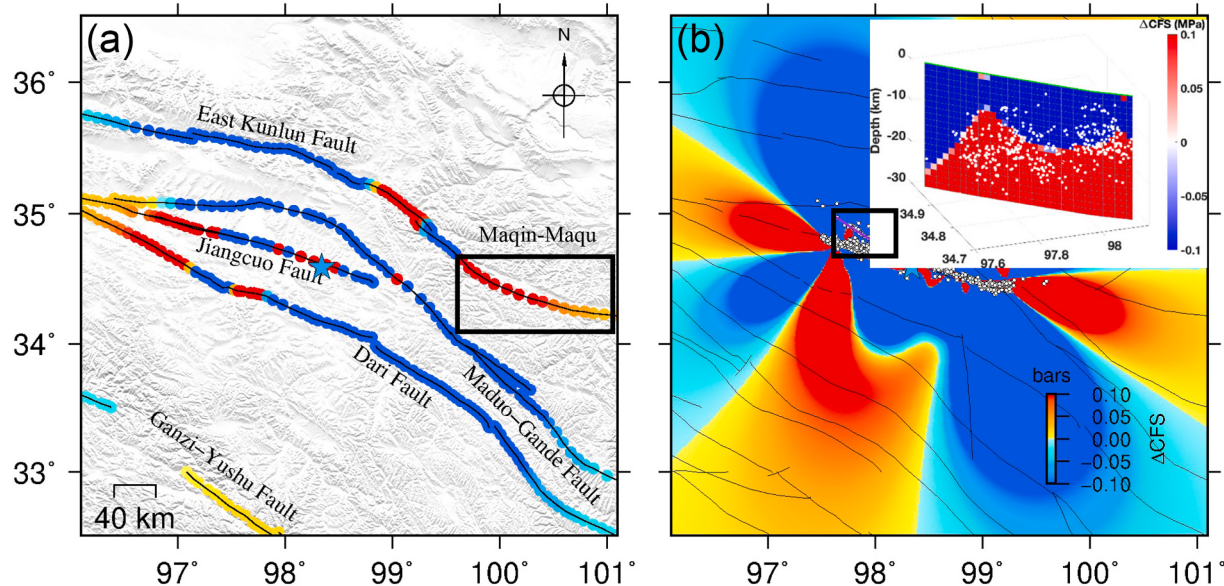


**Fig. 10.** (a) Co-seismic  $\Delta$ CFS on the four adjacent major faults caused by the 2021  $M_w$  7.4 Maduo earthquake. The Maqin–Maqu Fault section, which is part of the East Kunlun Fault, is denoted by the black rectangular frame. (b) The co-seismic Coulomb stress changes on the horizontal plane at a 10-km depth, where the white dots indicate the distribution of the aftershock sequences. The blue star denotes the epicenter. The insert map shows the co-seismic  $\Delta$ CFS at the depth of the aftershock sequence fault caused by the main shock, and the white dots are the aftershocks on this fault. (For interpretation of the references to colour in this figure legend, the reader is referred to the web version of this article.)

## 5. Conclusions

In this study, we investigated the source kinematics of the 2021  $M_w$  7.4 Maduo earthquake using the 1-Hz GNSS displacement waveforms, GNSS static offsets and the 3D displacements obtained by an improved TR-ESISTEM algorithm based on the SAR observations. Our preferred slip model indicates that this event spread bilaterally with asymmetric rupture velocities: 3.8 km/s to the southeast of epicenter and 2.2 km/s to the northwest, and the overall average rupture velocity was 2.8 km/s. Bulk of slip was formed to the southeast of the epicenter within a 10 km depth while to the northwest the slip concentration is a bit shallow to above 6 km. The source time function showed a total duration of  $\sim 35$  s, with  $1.61 \times 10^{20}$  Nm seismic moment released in total. Strong motion simulation shows the acceleration caused by the earthquake exceeded the building code limits for several bridges that collapsed due to strong ground shaking. The variation of the static Coulomb stress in the neighboring strike-slip faults indicates that this event mainly released the stress accumulation on the eastern Kunlun boundary and several secondary faults in the Bayan Har block, and accelerated the stress accumulation in the Maqin–Maqu section of the East Kunlun Fault. The increased stress level on a possible fault branch, which was not detected by the InSAR interferograms, caused the occurrence of the aftershock sequence six hours after the main shock at depth 10–25 km.

## Credit author statement

**Mingzhe Lyu:** Data curation, Investigation, Methodology, Resources, Validation, Visualization, Writing original draft. **Kejie Chen:** Conceptualization, Formal analysis, Writing original draft, Writing review & editing, Supervision, Funding acquisition. **Changhu Xue:** Data curation. **Nan Zang:** Formal analysis. **Wei Zhang:** Review & editing; **Guoguang Wei:** Data curation.

## Declaration of Competing Interest

The authors declare that they have no known competing financial interests or personal relationships that could have appeared to influence the work reported in this paper.

## Data availability

Data will be made available on request.

## Acknowledgement

We would like to thank Xiaohua Xu, Cunren Liang, and Yangmao Wen for their suggestions about InSAR data processing. Constructive remarks from three anonymous reviewers and Editor Ling Chen improve the manuscript greatly. This work was supported by the National Natural Science Foundation of China (Grant Nos. 42074024 and U1901602). The Sentinel-1A and Sentinel-1B SAR data were provided by the European Space Agency. The 1-Hz GNSS displacement waveforms were provided by Chen et al. (2022). Some figures in this paper were drawn by the use of Generic Mapping Tools (GMT) software (Wessel et al., 2013).

## Appendix A. Supplementary data

Supplementary data to this article can be found online at <https://doi.org/10.1016/j.tecto.2022.229542>.

## References

- Agram, P.S., Zebker, H.A., 2009. Sparse two-dimensional phase unwrapping using regular-grid methods. *IEEE Geosci. Remote Sens. Lett.* 6 (2), 327–331. <https://doi.org/10.1109/LGRS.2009.2012445>.
- Akaike, H., 1980. Likelihood and the Bayes procedure. *Trab. Estad. Investig. Oper.* 31 (1), 143–166.
- Avouac, J.-P., Tappin, P., 1993. Kinematic model of active deformation in central Asia. *Geophys. Res. Lett.* 20 (10), 895–898. <https://doi.org/10.1029/93GL00128>.
- Borre, K., 2007. *Elasticity and Stress-Strain Relations in Geodetic Networks*. Bollettino Di Geodesia e Scienze Affini, XXXVIII, pp. 417–456.
- Bruhat, L., Fang, Z., Dunham, E.M., 2016. Rupture complexity and the supershear transition on rough faults. *J. Geophys. Res. Solid Earth* 121 (1), 210–224. <https://doi.org/10.1002/2015JB012512>.
- Chen, C.W., Zebker, H.A., 2000. Network approaches to two-dimensional phase unwrapping: intractability and two new algorithms. *JOSA A* 17 (3), 401–414. <https://doi.org/10.1364/JOSAA.17.000401>.
- Chen, K., Avouac, J.-P., Geng, J., Liang, C., Zhang, Z., Li, Z., Zhang, S., 2022. The 2021  $M_w$  7.4 Maduo earthquake: an archetype bilateral slip-pulse rupture arrested at a

- splay fault. *Geophys. Res. Lett.* 49 (2), e2021GL095243 <https://doi.org/10.1029/2021GL095243>.
- Da, Huaguan, 1983. On the dari earthquake of 1947 in Qinghai Province. *Northwestern Seismol. J.* 03, 71–77.
- Ekström, G., Nettles, M., Dziewoński, A.M., 2012. The global CMT project 2004–2010: centroid-moment tensors for 13,017 earthquakes. *Phys. Earth Planet. Inter.* 200–201, 1–9. <https://doi.org/10.1016/j.pepi.2012.04.002>.
- Farr, T.G., Rosen, P.A., Caro, E., Crippen, R., Duren, R., Hensley, S., et al., 2007. The shuttle radar topography mission. *Rev. Geophys.* 45 (2) <https://doi.org/10.1029/2005RG000183>.
- Feng, W., Tian, Y., Zhang, Y., Samsonov, S., Almeida, R., Liu, P., 2017. A slip gap of the 2016 Mw 6.6 Muji, Xinjiang, China, earthquake inferred from sentinel-1 TOPS interferometry. *Seismol. Res. Lett.* 88 (4), 1054–1064. <https://doi.org/10.1785/0220170019>.
- Fialko, Y., Simons, M., Agnew, D., 2001. The complete (3-D) surface displacement field in the epicentral area of the 1999 Mw7.1 Hector Mine earthquake, California, from space geodetic observations. *Geophys. Res. Lett.* 28 (16), 3063–3066.
- Fialko, Y., Sandwell, D., Simons, M., Rosen, P., 2005. Three-dimensional deformation caused by the Bam, Iran, earthquake and the origin of shallow slip deficit. *Nature* 435 (7040), 295–299. <https://doi.org/10.1038/nature03425>.
- Gai, H., Yao, S., Yang, L., Kang, T., Yin, X., Chen, T., Li, X., 2021. Coseismic surface rupture characteristics, causes and significance of the “5.22” Ms 7.4 earthquake in Maduo, Qinghai. *J. Geom.* 27 (6), 1–19. Retrieved from. <https://kns.cnki.net/kcms/detail/detail.aspx?dbcode=CAPJ&dbname=CAPJLAST&filename=DZLX20201812001&uniplatform=NZKPT&v=mWdQTBu%25mmd2Fs3UOMAQmo6dd7hu81tbAVPHHW1XfJ3aMqKI%25mmd2B%25mmd2FC%25mmd2F6NF9YduYLPAae7Se>.
- Guan, Zhongguo, Huang, Yong, Zhang, Haoyu, Gai, Hailong, Cai, Liwen, Zhan, Beilei, Liu, Wei, 2021. Damage characteristics and analysis of bridge engineering in M7.4 Qinghai Maduo earthquake. *World Earthq. Eng.* 37 (03), 38–45.
- Guglielmino, F., Nunnari, G., Puglisi, G., Spata, A., 2011. Simultaneous and integrated strain tensor estimation from geodetic and satellite deformation measurements to obtain three-dimensional displacement maps. *IEEE Trans. Geosci. Remote Sens.* 49 (6), 1815–1826. <https://doi.org/10.1109/TGRS.2010.2103078>.
- Guo, R., Yang, H., Li, Y., Zheng, Y., Zhang, L., 2021. Complex Slip distribution of the 2021 Mw 7.4 Maduo, China, earthquake: an Event Occurring on the Slowly Slipping Fault. *Seismol. Res. Lett.* <https://doi.org/10.1785/0220210226>.
- Hansen, P.C., 1990. Truncated singular value decomposition solutions to discrete ill-posed problems with ill-determined numerical rank. *SIAM J. Sci. Stat. Comput.* 11 (3), 503–518. <https://doi.org/10.1137/0911028>.
- Hansen, P.C., 1992. Analysis of discrete ill-posed problems by means of the L-curve. *SIAM Rev.* 34 (4), 561–580. <https://doi.org/10.1137/1034115>.
- Hartzell, S.H., Heaton, T.H., 1983. Inversion of strong ground motion and teleseismic waveform data for the fault rupture history of the 1979 Imperial Valley, California, earthquake. *Bull. Seismol. Soc. Am.* 73 (6A), 1553–1583. <https://doi.org/10.1785/BSSA07306A1553>.
- He, L., Feng, G., Wu, X., Lu, H., Xu, W., Wang, Y., et al., 2021. Coseismic and early postseismic slip models of the 2021 Mw 7.4 Maduo earthquake (Western China) estimated by space-based geodetic data. *Geophys. Res. Lett.* 48 (24) <https://doi.org/10.1029/2021GL095860> e2021GL095860.
- Hu, J., Li, Z.-W., Li, J., Zhang, L., Ding, X.-L., Zhu, J.-J., Sun, Q., 2014. 3-D movement mapping of the alpine glacier in Qinghai-Tibetan Plateau by integrating D-InSAR, MAI and Offset-Tracking: case study of the Dongkemadi Glacier. *Glob. Planet. Chang.* 118, 62–68. <https://doi.org/10.1016/j.gloplacha.2014.04.002>.
- Jin, Z., Fialko, Y., 2021. Coseismic and early postseismic deformation due to the 2021 M7.4 Maduo (China) earthquake. *Geophys. Res. Lett.* 48 (21) <https://doi.org/10.1029/2021GL095213>.
- Jónsson, S., Zebker, H., Segall, P., Amelung, F., 2002. Fault slip distribution of the 1999 Mw 7.1 Hector Mine, California, earthquake, estimated from satellite radar and GPS measurements. *Bull. Seismol. Soc. Am.* 92 (4), 1377–1389.
- Kim, A., Dreger, D.S., 2008. Rupture process of the 2004 Parkfield earthquake from near-fault seismic waveform and geodetic records. *J. Geophys. Res. Solid Earth* 113 (B7). <https://doi.org/10.1029/2007JB005115>.
- King, G.C.P., Stein, R.S., Lin, J., 1994. Static stress changes and the triggering of earthquakes. *Bull. Seismol. Soc. Am.* 84 (3), 935–953.
- Laske, G., Masters, G., Ma, Z., Pasquenos, M., 2013. Update on CRUST1.0—A 1-degree global model of Earth's crust. *Geophys. Res. Abstr.* 15, 2658.
- Lawson, C.L., Hanson, R.J., 1995. Solving least squares problems. SIAM 15.
- Li, Z., Ding, K., Zhang, P., Wen, Y., Zhao, L., Chen, J., 2021. Co-seismic Deformation and Slip Distribution of 2021 Mw 7.4 Madou Earthquake From GNSS Observation. *Geomatics and Information Science of Wuhan University*, pp. 1–10. <https://doi.org/10.13203/j.whgis20210301>.
- Li, Q., Wan, Y., Li, C., Tang, H., Tan, K., Wang, D., 2022. Source process featuring asymmetric rupture velocities of the 2021 Mw 7.4 Maduo, China, earthquake from teleseismic and geodetic data. *Seismol. Res. Lett.* 93 (3), 1429–1439. <https://doi.org/10.1785/0220210300>.
- Lin, J., Stein, R.S., 2004. Stress triggering in thrust and subduction earthquakes and stress interaction between the southern San Andreas and nearby thrust and strike-slip faults. *J. Geophys. Res. Solid Earth* 109 (B2). <https://doi.org/10.1029/2003JB002607>.
- Luo, H., Chen, T., 2016. Three-dimensional surface displacement field associated with the 25 April 2015 Gorkha, Nepal, earthquake: solution from integrated InSAR and GPS measurements with an extended SISTEM approach. *Remote Sens.* 8 (7), 559. <https://doi.org/10.3390/rs8070559>.
- Mehrabi, H., Vosoghi, B., Motagh, M., Hanssen, R.F., 2019. Three-dimensional displacement fields from InSAR through Tikhonov regularization and least-squares variance component estimation. *J. Surv. Eng.* 145 (4), 04019011. [https://doi.org/10.1061/\(ASCE\)SU.1943-5428.0000289](https://doi.org/10.1061/(ASCE)SU.1943-5428.0000289).
- Melgar Moctezuma, D., 2014. Seismogeodesy and Rapid Earthquake and Tsunami Source Assessment. Retrieved from. <http://adsabs.harvard.edu/abs/2014PhDT.....219M>.
- Melgar, D., Geng, J., Crowell, B.W., Haase, J.S., Bock, Y., Hammond, W.C., Allen, R.M., 2015. Seismogeodesy of the 2014 Mw6.1 Napa earthquake, California: rapid response and modeling of fast rupture on a dipping strike-slip fault. *J. Geophys. Res. Solid Earth* 120 (7), 5013–5033. <https://doi.org/10.1002/2015JB011921>.
- Melgar, D., Ganas, A., Taymaz, T., Valkaniotis, S., Crowell, B.W., Kapetanidis, V., et al., 2020. Rupture kinematics of 2020 January 24 Mw 6.7 Doganöly-Sivrice, Turkey earthquake on the East Anatolian Fault Zone imaged by space geodesy. *Geophys. J. Int.* 223 (2), 862–874. <https://doi.org/10.1093/gji/ggaa345>.
- Ministry of Transportation of China, 2020. Specifications for Seismic Design of Highway Bridges (JTG/T 2231-01-2020). China Communications Publishing Beijing.
- Okada, Y., 1992. Internal deformation due to shear and tensile faults in a half-space. *Bull. Seismol. Soc. Am.* 82 (2), 1018–1040. <https://doi.org/10.1785/BSSA0820021018>.
- Pietrantonio, G., Riguzzi, F., 2004. Three-dimensional strain tensor estimation by GPS observations: methodological aspects and geophysical applications. *J. Geodyn.* 38 (1), 1–18. <https://doi.org/10.1016/j.jog.2004.02.021>.
- Ren, J., Xu, X., Zhang, G., Wang, Q., Zhang, Z., Gai, H., Kang, W., 2022. Coseismic surface ruptures, slip distribution, and 3D seismogenic fault for the 2021 Mw 7.3 Maduo earthquake, central Tibetan Plateau, and its tectonic implications. *Tectonophysics* 827, 229275. <https://doi.org/10.1016/j.tecto.2022.229275>.
- Rosen, P.A., Gurrola, E., Sacco, G.F., Zebker, H., 2012. The InSAR scientific computing environment. In: *EUSAR 2012; 9th European Conference on Synthetic Aperture Radar*, pp. 730–733.
- Sandwell, D., Mellors, R., Tong, X., Wei, M., Wessel, P., 2011. GMTSAR: An InSAR Processing System Based on Generic Mapping Tools. Retrieved from. <https://eschoolarship.org/uc/item/8zq2c02m>.
- Shan, B., Xiong, X., Wang, R., Zheng, Y., Yadav, R.B.S., 2015. Stress evolution and seismic hazard on the Maqin-Maqu segment of East Kunlun Fault zone from co-, post- and interseismic stress changes. *Geophys. J. Int.* 200 (1), 244–253. <https://doi.org/10.1093/gji/ggu395>.
- Tikhonov, A.N., 1963. Solution of incorrectly formulated problems and the regularization method. *Sov. Math.* 4, 1035–1038.
- Tikhonov, A.N., Goncharsky, A.V., Stepanov, V.V., Yagola, A.G., 2013. Numerical Methods for the Solution of Ill-Posed Problems, 328. Springer Science & Business Media.
- Vaka, D.S., Rao, Y.S., Singh, T., 2020. Surface deformation of the 2019 Mirpur earthquake estimated from sentinel-1 InSar data. In: *2020 IEEE India Geoscience and Remote Sensing Symposium (InGARSS)*, pp. 130–133. <https://doi.org/10.1109/InGARSS48198.2020.9358915>.
- Wang, K., Fialko, Y., 2014. Space geodetic observations and models of postseismic deformation due to the 2005 M7.6 Kashmir (Pakistan) earthquake. *J. Geophys. Res. Solid Earth* 119 (9), 7306–7318. <https://doi.org/10.1002/2014JB011122>.
- Wang, D., Mori, J., Koketsu, K., 2016. Fast rupture propagation for large strike-slip earthquakes. *Earth Planet. Sci. Lett.* 440, 115–126. <https://doi.org/10.1016/j.epsl.2016.02.022>.
- Wang, W., Fang, L., Wu, J., Tu, H., Chen, L., Lai, G., Zhang, L., 2021a. Aftershock sequence relocation of the 2021 Ms7.4 Maduo Earthquake, Qinghai, China. *Sci. China Earth Sci.* 1–10.
- Wang, M., Wang, F., Jiang, X., Tian, J., Li, Y., Sun, J., Shen, Z.-K., 2021b. GPS determined coseismic slip of the 2021 Mw7.4 Maduo, China, earthquake and its tectonic implication. *Geophys. J. Int.* 228 (3), 2048–2055. <https://doi.org/10.1093/gji/ggab460>.
- Wen, X., Yi, G., Xu, X., 2007. Background and precursory seismicities along and surrounding the Kunlun fault before the Ms8.1, 2001, Kokoxili earthquake, China. *J. Asian Earth Sci.* 30 (1), 63–72. <https://doi.org/10.1016/j.jseas.2006.07.008>.
- Wessel, P., Smith, W.H., Scharroo, R., Luis, J., Wobbe, F., 2013. Generic mapping tools: improved version released. *EOS Trans. Am. Geophys. Union* 94 (45), 409–410.
- Xu, X., Tong, X., Sandwell, D.T., Milliner, C.W.D., Dolan, J.F., Hollingsworth, J., et al., 2016. Refining the shallow slip deficit. *Geophys. J. Int.* 204 (3), 1867–1886. <https://doi.org/10.1093/gji/ggv563>.
- Yue, H., Zhang, Y., Ge, Z., Wang, T., Zhao, L., 2020. Resolving rupture processes of great earthquakes: reviews and perspective from fast response to joint inversion. *Sci. China Earth Sci.* 63 (4), 492–511. <https://doi.org/10.1007/s11430-019-9549-1>.
- Yue, H., Shen, Z.-K., Zhao, Z., Wang, T., Cao, B., Li, Z., et al., 2022. Rupture process of the 2021 M7.4 Maduo earthquake and implication for deformation mode of the Songpan-Ganzi terrane in Tibetan Plateau. *Proc. Natl. Acad. Sci.* 119 (23), e2116445119. <https://doi.org/10.1073/pnas.2116445119>.
- Zhang, W., Chen, X., 2006. Traction image method for irregular free surface boundaries in finite difference seismic wave simulation. *Geophys. J. Int.* 167 (1), 337–353. <https://doi.org/10.1111/j.1365-246X.2006.03113.x>.
- Zhang, X., Feng, W., Du, H., Samsonov, S., Yi, L., 2022a. Supershear rupture during the 2021 MW 7.4 Maduo, China, earthquake. *Geophys. Res. Lett.* 49 (6) <https://doi.org/10.1029/2022GL097984>.
- Zhang, J., Wang, X., Chen, L., Liu, J., 2022b. Seismotectonics and fault geometries of the Qinghai Maduo Ms7.4 earthquake sequence: insight from aftershock relocations and

- focal mechanism solutions. Chin. J. Geophys. 65 (2), 552–562. <https://doi.org/10.6038/cjg2022P0516>.
- Zhao, D., Qu, C., Chen, H., Shan, X., Song, X., Gong, W., 2021. Tectonic and geometric control on fault kinematics of the 2021 Mw7.3 Maduo (China) earthquake inferred from interseismic, coseismic, and postseismic InSAR observations. Geophys. Res. Lett. 48 (18) <https://doi.org/10.1029/2021GL095417> e2021GL095417.
- Zhu, L., Rivera, L.A., 2002. A note on the dynamic and static displacements from a point source in multilayered media. Geophys. J. Int. 148 (3), 619–627. <https://doi.org/10.1046/j.1365-246X.2002.01610.x>.